Flagellum couples cell shape to motility in *Trypanosoma brucei*

Stella Y. Sun[a,b,c], Jason T. Kaelber[d], Muyuan Chen[e], Xiaoduo Dong[f], Yasaman Nematbakhsh[g], Jian Shi[h], Matthew Dougherty[e], Chwee Teck Lim[f,g], Michael F. Schmid[c], Wah Chiu[a,b,c,1], and Cynthia Y. He[f,h,1]

[a]Department of Bioengineering, James H. Clark Center, Stanford University, Stanford, CA 94305; [b]Department of Microbiology and Immunology, James H. Clark Center, Stanford University, Stanford, CA 94305; [c]SLAC National Accelerator Laboratory, Stanford University, Menlo Park, CA 94025; [d]Department of Molecular Virology and Microbiology, Baylor College of Medicine, Houston, TX 77030; [e]Verna and Marrs McLean Department of Biochemistry and Molecular Biology, Baylor College of Medicine, Houston, TX 77030; [f]Mechanobiology Institute, National University of Singapore, Singapore 117411; [g]Department of Mechanical Engineering, National University of Singapore, Singapore 117575; and [h]Department of Biological Sciences, Center for BioImaging Sciences, National University of Singapore, Singapore 117543

Contributed by Wah Chiu, May 17, 2018 (sent for review December 29, 2017; reviewed by Phillipe Bastin and Abraham J. Koster)

In the unicellular parasite *Trypanosoma brucei,* the causative agent of human African sleeping sickness, complex swimming behavior is driven by a flagellum laterally attached to the long and slender cell body. Using microfluidic assays, we demonstrated that *T. brucei* can penetrate through an orifice smaller than its maximum diameter. Efficient motility and penetration depend on active flagellar beating. To understand how active beating of the flagellum affects the cell body, we genetically engineered *T. brucei* to produce anucleate cytoplasts (zoids and minis) with different flagellar attachment configurations and different swimming behaviors. We used cryo-electron tomography (cryo-ET) to visualize zoids and minis vitrified in different motility states. We showed that flagellar wave patterns reflective of their motility states are coupled to cytoskeleton deformation. Based on these observations, we propose a mechanism for how flagellum beating can deform the cell body via a flexible connection between the flagellar axoneme and the cell body. This mechanism may be critical for *T. brucei* to disseminate in its host through size-limiting barriers.

cell deformation | flagellum | cell motility | *Trypanosoma brucei* | cryo-electron tomography

Trypanosomes, including *Trypanosoma brucei*, *Trypanosoma cruzi*, and *Leishmania* spp., are single-celled parasites that infect millions of people. The World Health Organization has recognized that trypanosomes cause several "neglected tropical diseases" (1). The multistage life cycle of these pathogens alternates between mammalian and insect hosts. Survival and transmission of these parasitic organisms critically depend on cell motility. In *T. brucei,* cell motility is driven by a flagellum attached laterally along the cell body (2). The molecular basis of flagellum attachment has been investigated by biochemical and molecular genetics methods (3–7). These studies highlight the functional importance of the flagellum attachment in flagella-driven cell motility and flagella-regulated cell morphogenesis during the parasite cell cycle and life cycle development. Cell motility has been studied by high-speed video microscopy and simulation methods (8–12). These studies provided important mechanistic insights into the flagellum-dependent cell motility and emphasized the strong influence of environmental conditions on cell motility. For example, the mammalian bloodstream form of parasites exhibit faster, more directional movement in a crowded and high-viscosity medium, mimicking the blood (8). When cultured on agar plates, the procyclic, insect-stage parasites demonstrate social motility behavior that is not observed in cell suspensions (13). From these early studies, it is plausible to hypothesize that both flagellum beating and host environments might affect the parasites' motility behavior. However, due to the resolution limitation of light microscopy, information on 3D ultrastructural organization of the cell body and its structural and functional coupling to flagellar beating is still lacking.

Cryo-electron tomography (cryo-ET) allows us to view 3D supramolecular details of biological samples preserved in their proper cellular context without chemical fixative and/or metal stain. However, samples thicker than 1 μm are not accessible to cryo-ET because at typical accelerating voltages (≤300 kV), few singly scattered electrons would penetrate such a thick sample (14). Therefore, cryo-ET of an entire intact eukaryote has not been feasible except in some cases, such as picoplankton (15), *Plasmodium* sporozoites (16), and human platelets (17), which have no nucleus.

The procyclic form of *T. brucei* has a long and slender shape with a maximum diameter of 2–3 μm near the nucleus (18, 19). Its characteristic auger shape is generated by a subpellicular microtubule (SPM) array consisting of >100 stable microtubules cross-linked with each other and with the inner face of the plasma membrane to form a cage-like scaffold beneath the cell membrane (20–22) (*SI Appendix*, Fig. S1*A*). The membrane-bound flagellum contains a microtubular axoneme and a paraflagellar rod (PFR) that exits the cell body and extends toward the anterior, tapered end of the cell (*SI Appendix*, Fig. S1*B*). The extracellular part of the flagellum is attached via its membrane laterally to the cell body, primarily as a left-handed helix (22, 23). Previous ET studies showed regularly spaced, staple-like structures along the flagellum

Significance

***Trypanosoma brucei* is a highly invasive pathogen capable of penetrating deeply into host tissues. To understand how flagellar motility facilitates cell penetration, we used cryo-electron tomography (cryo-ET) to visualize two genetically anucleate mutants with different flagellar motility behaviors. We found that the *T. brucei* cell body is highly deformable as defined by changes in cytoskeletal twist and spacing, in response to flagellar beating and environmental conditions. Based on the cryo-ET models, we proposed a mechanism of how flagellum motility is coupled to cell shape changes, which may facilitate penetration through size-limiting barriers.**

Author contributions: W.C. and C.Y.H. designed research; S.Y.S., X.D., and J.S. performed research; S.Y.S., M.D., and M.F.S. contributed new reagents/analytic tools; S.Y.S., J.T.K., M.C., Y.N., C.T.L., and M.F.S. analyzed data; and S.Y.S., J.T.K., M.F.S., W.C., and C.Y.H. wrote the paper.

Reviewers: P.B., Institut Pasteur; and A.J.K., Leiden University Medical Center.

The authors declare no conflict of interest.

This open access article is distributed under Creative Commons Attribution-NonCommercial-NoDerivatives License 4.0 (CC BY-NC-ND).

Data deposition: The data reported in this paper have been deposited in the Electron Microscopy Data Bank (accession numbers EMD-6748, EMD-6749, and EMD-6750).

[1]To whom correspondence may be addressed. Email: wahc@stanford.edu or dbshyc@nus.edu.sg.

This article contains supporting information online at www.pnas.org/lookup/suppl/doi:10.1073/pnas.1722618115/-/DCSupplemental.

Published online June 11, 2018.

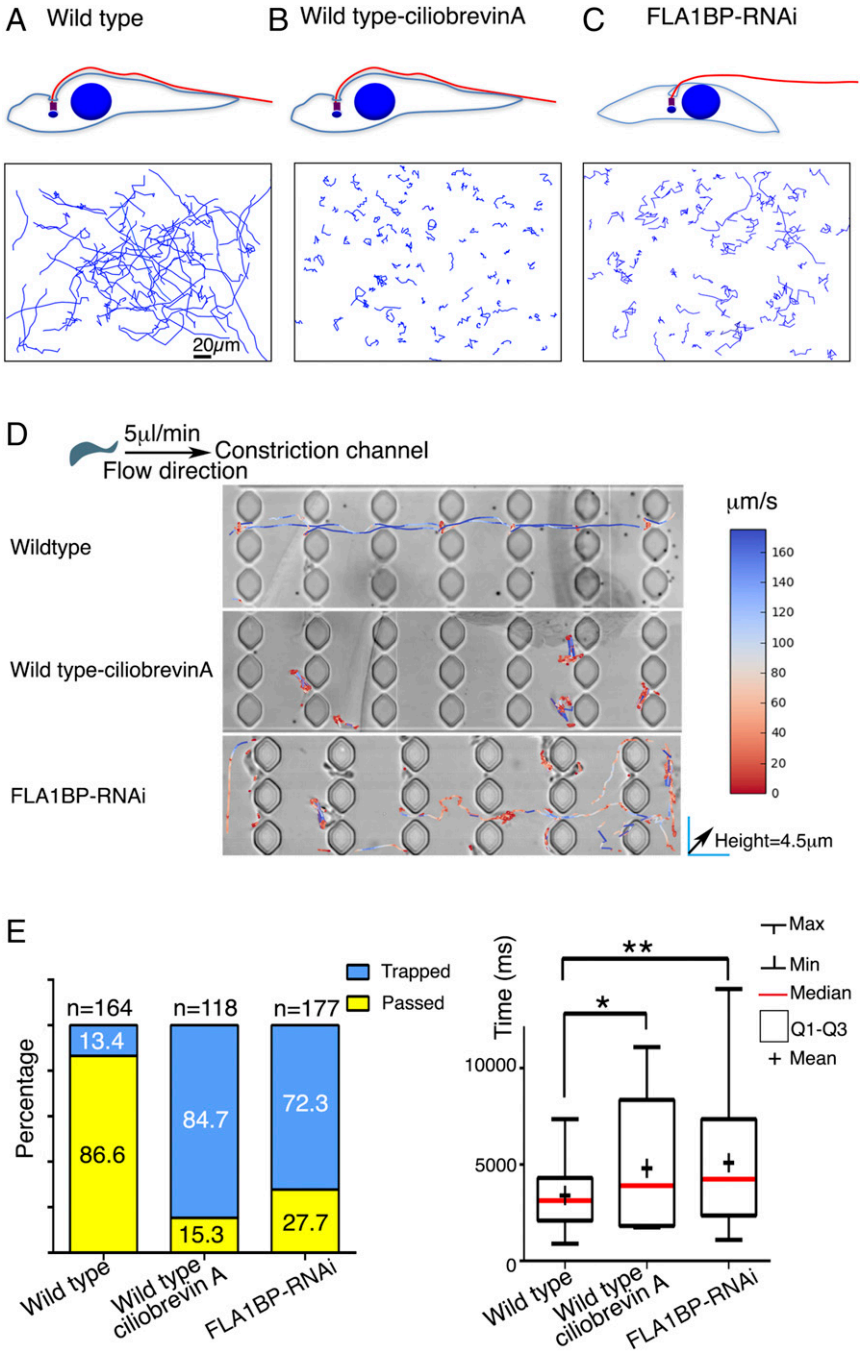

Fig. 1. Coordinated flagellum–cell body movement facilitates cell deformation and passage through size-limiting microfluidic devices. (*A*–*C*) Wild-type, FLA1BP-RNAi, and ciliobrevin A-treated cells differ in flagellum attachment and motility behaviors ($n \sim 90$ for each). (*D*) Wild-type, with or without ciliobrevin A treatment, and FLA1BP-RNAi cells were passed through the constriction channels with 1.4-μm orifices at a constant flow rate of 5 μL/min and recorded at 100 fps for 13 s. Traces of cell movement are shown overlaying the microfluidic chamber, with colors representing different velocities. (*E*) The percentage of cells, able to pass through at least 10 consecutive constricting orifices within the 13 s of imaging time, was monitored (*Left*), and the total time required to pass through 10 consecutive orifices was determined for each cell (*Right*). *P* value is calculated by two-tailed unpaired *t* test: $*P < 0.05$ and $**P < 0.01$.

that connect the flagellar and cell body membranes (24) (*SI Appendix*, Fig. S1*C*). Other electron-dense filament-like structures have been seen between the flagellum and the SPMs (22). Four special SPMs, called the microtubule quartet (MtQ), are nucleated near the basal bodies, run along the flagellar attachment zone, and are antiparallel to all other SPMs.

Using microfluidic devices, we found that procyclic *T. brucei* cells are capable of penetrating size-limiting orifices smaller than their maximum cell diameter. Inhibition of flagellar beating and perturbation of flagellar attachment both impair the cell's ability to penetrate, suggesting a role of flagellar motility in modifying the cell body. To characterize cell body structural changes associated with *T. brucei* cell movement, we genetically engineered anucleate *T. brucei*, which allowed us to examine the whole cytoskeleton in three dimensions using cryo-ET without sectioning or milling. Changes in SPM twist and SPM spacing were found to associate with the flagellar pattern known to correlate with its beating, indicating that the SPM is highly deformable (at least in its

twist angle) in response to flagellar beating and/or environmental conditions. By comparing 3D annotated tomograms of parasites with different flagellar attachment and cell motility patterns, we generated a model to explain how flagellar beating, together with environment conditions, can induce cell body deformation.

Results

Coordinated Flagellum–Cell Body Movement Facilitates Cell Passage Through a Size-Limiting Microfluidic Array. *T. brucei* can penetrate deep tissues and other physical barriers during host infections (2). To investigate the migration behavior, procyclic *T. brucei* cells in culture medium were passed through a microfluidic device with arrays of 1.4-μm slits, at a constant flow rate of 5 μL/min (Fig. 1 and *SI Appendix*, Fig. S2). Under this condition, the directional migration of the cells through the microfluidic device was driven by the flow rather than the directional motility of the cell. The maximum unhindered velocity of cells in the microfluidic device was measured to be ∼160 μm/s, shown in Fig. 1*D*. The 1.4-μm slit width is approximately one-half the maximum diameter of an average procyclic cell; thus, the ability of a cell to pass through the size-limiting slits and the time required to do so reflected how well the cell could compress or deform at the orifices.

Impressively, greater than 85% of wild-type cells could pass through at least 10 consecutive size-limiting slits during the 13-s recording time (Movie S1), suggesting deformability of the cell body. To evaluate the role of flagellar motility in this penetration behavior, we perturbed flagellar motility in two different ways. First, *T. brucei* cells were treated with a dynein inhibitor ciliobrevin A, which has been shown to significantly inhibit *Leishmania* flagellar beating and coordinated cell movement (25). In the second approach, cells were depleted of FLA1BP, a membrane adhesion molecule involved in flagellar attachment (26), by tetracycline-inducible RNAi (*SI Appendix*, Fig. S3*A*). FLA1BP-RNAi cells are viable and proliferate normally in cell culture, despite flagellar detachment from the cell body (26). Cell motility was significantly impaired in both ciliobrevin A-treated and FLA1BP-RNAi cells (Fig. 1 *A*–*C*).

Under the same flow conditions, only ∼15% of ciliobrevin A-treated cells and ∼27% of FLA1BP-RNAi cells were able to pass through at least 10 consecutive size-limiting slits during the 13-s recording time (Fig. 1 *D* and *E* and Movie S1). Of the cells that completed the passage, ciliobrevin A-treated and FLA1BP-RNAi cells both took longer than wild-type cells to traverse the same distance. Together, these results suggest that flagellum-driven, attachment-mediated motility facilitates cell passage through size-limiting barriers, and may require deformation of live trypanosome cells. To further explore this possibility, we went on to examine the motility-associated changes in the cell body using cryo-ET at nanometer resolution scale.

Generation of Anucleate *T. brucei* with Different Flagellum Attachment and Motility Phenotypes. *T. brucei* nuclei are large and located at the widest part of the cell (18, 19). Thus, we genetically engineered a thinner anucleate *T. brucei* (also known as a "zoid") that could be suitable for cryo-ET. Zoids are generated by inhibiting nuclear division either through the use of anti-microtubule drugs (27) or genetic perturbation (28, 29). We used RNAi silencing of TbCentrin4 to induce zoid formation. This silencing led to unequal nuclei segregation into daughter cells, producing both anucleate and multinucleate daughters (29) (Fig. 2*A*). Compared with other zoid-inducing methods, TbCentrin4-RNAi has several advantages. Zoids produced by TbCentrin4-RNAi had normal flagellar attachment, were motile, and retained the long and slender cell shape as in wild-type cells (29) (Figs. 2 and 3 and *SI Appendix*, Fig. S3*B*). Additionally, TbCentrin4-RNAi did not inhibit nuclear division in nucleate daughter cells. Continued nuclear division generated large numbers of both zoids and multinucleated cells. These two cell types were easily separated using cell sorting or differential centrifugation (29).

In addition to zoids, we generated anucleate *T. brucei* having a detached flagellum, referred to as minis. Minis were generated by silencing both TbCentrin4 and FLA1BP (*SI Appendix*, Fig. S3*A*). Both zoids and minis had flagella of similar length to that of wild-type cells (Fig. 2*A*). With the exception of the nucleus, they contained all of the other major organelles examined (29)

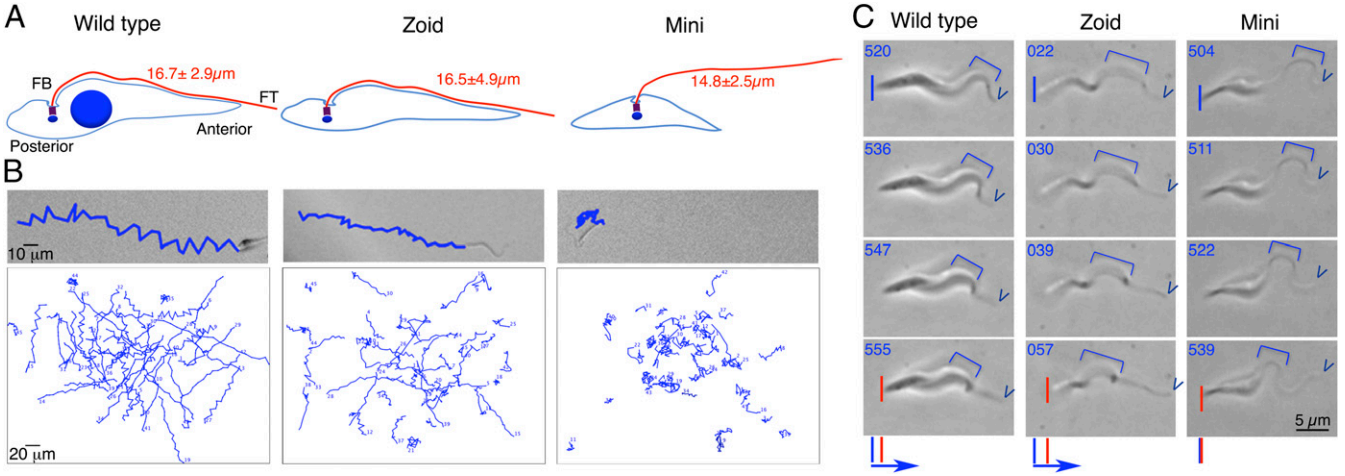

Fig. 2. Anucleate zoids and minis exhibit different flagellum attachment configurations and motility behaviors. (*A*) Comparison of cellular organization in zoids and minis relative to wild-type cells. Both minis and zoids lack a nucleus (depicted by the big blue circle) but contain other major organelles, including the kinetoplast (small blue circle), the basal bodies (purple square), and the flagellum (red line). The flagellum was of similar length in all three types ($n \sim 100$ for each): 16.7 ± 2.9 μm for wild type, 16.5 ± 4.9 μm for zoids, and 14.8 ± 2.5 μm for minis. FB, flagellar base; FT, flagellar tip. (*B*) Live-cell movement was recorded by videomicroscopy (∼6 fps) and analyzed by manual tracking of the posterior end using ImageJ ($n = 45$ for each). (*C*) Flagellar beating and movement of wild type, zoids, and minis were recorded with high-speed videomicroscopy at 1,000 fps. In all types, most flagellar waves (brackets) initiated from near the distal tip of the flagellum (arrowheads) and propagated along the flagellum toward the flagellar base. The positions of the posterior end near the beginning and end of a wave propagation are marked by blue and red lines, respectively. Numbers in the *Top Left* corner indicate time in milliseconds. Arrows indicate the direction of movement.

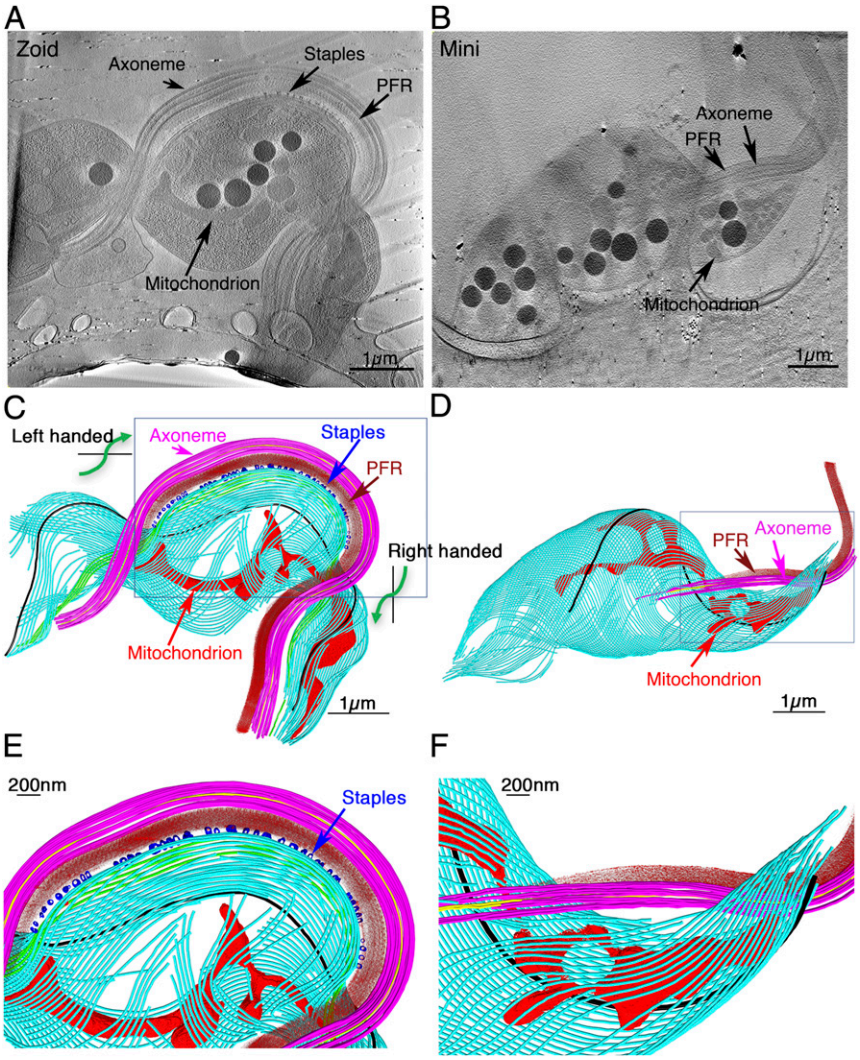

Fig. 3. Three-dimensional manually annotated tomograms of a representative zoid and mini. (*A* and *B*) A representative slice of reconstructed tomograms for the zoid (*A*) and the mini (*B*). (*C* and *D*) Manual annotations of subcellular features in a representative zoid (*C*) and mini (*D*). *E* and *F* are enlarged views of the boxed areas in *C* and *D*, respectively. Axoneme, purple; PFR, dark red; staples, blue; mitochondria, red; SPMs, cyan; and MtQ microtubules, green. One single SPM in the zoid and the mini was colored black. Note that compression of the samples was observed in some cases, resulting in flattened appearance of the samples as seen in the 3D maps. Missing wedge and flattening may also account for the absence (in certain orientations) and/or sharp bending of SPMs in some areas. However, such compression is expected in vivo as the cells pass through narrow spaces.

(*SI Appendix*, Fig. S3*B*). Anucleate mutants do not undergo further division, but they retained integrity and had actively beating flagella for at least 3 d in culture.

The motility of zoids and minis was analyzed by tracking the movement of individual cells using live-cell video microscopy (Fig. 2*B* and Movie S2) and high-speed video microscopy (Fig. 2*C*). As reported previously (8, 9), flagellar beating initiated mostly at the distal tip of the flagellum. In both wild-type cells and zoids, beating waves propagated along the flagellum and the attached cell body, toward the flagellar base, which propelled cell movement in the direction of the anterior end. In minis, both constant flagellar beating and tip-to-base propagating waves were observed similar to wild-type cells. However, their flagellar beating did not generate productive movement.

Cryo-ET of Zoids and Minis Reveal Differences in SPM Handedness. Zoids and minis were enriched to ∼70% homogeneity, vitrified, and imaged using an electron microscope (*Materials and Methods*). Tomograms of minis and zoids showed salient intracellular features, including the flagellum (with the axoneme and PFR), mitochondrion, and SPMs in orderly arrays (Fig. 3 *A* and *B* and Movies S3 and S4). Electron-dense granules of varying size of 100–350 nm in diameter were observed in both zoids and minis. Such structures were not reported in earlier cryo-ET cells and may be stress organelles or other unknown structures found in these anucleate mutants. Views of 3D annotated tomograms are shown in Fig. 3 *C* and *D* and Movies S3 and S4.

The overall shapes of both zoids and minis were similar to those of wild-type parasites, although minis were shorter due to the depletion of FLA1BP (Fig. 2*B*) (26). The flagellum of zoids was attached to the cell body. Electron-dense staple-like structures that connect the flagellar and cell membranes were localized to the attachment zone (Fig. 3 *C* and *E*). Staple-like structures were not observed in minis, in which the flagellum is detached from the plasma membrane (Fig. 3 *D* and *F*). This observation suggests that FLA1BP is a major component of the staple-like structures and/or that FLA1BP depletion prevents staple formation, assembly or stability.

The flagellum in some zoids exhibited a complex helical pattern along the cell body that formed a left-handed turn near the posterior end and a right-handed turn near the anterior end. To analyze SPM helicity and the effect of flagellar attachment, we annotated the flagella and SPMs in randomly selected tomograms of 12 minis and 25 zoids. In addition to manual annotations, we are able to reliably and confidently analyze the SPM configuration and flagellar handedness with a newly available automated tomogram annotation method (30). All 12 minis contained only left-handed SPM helices in the posterior part of the cell and left-handed or straight SPM toward the anterior, suggesting that left-handedness or straightness are probably the default configurations of the SPM in the absence of an attached

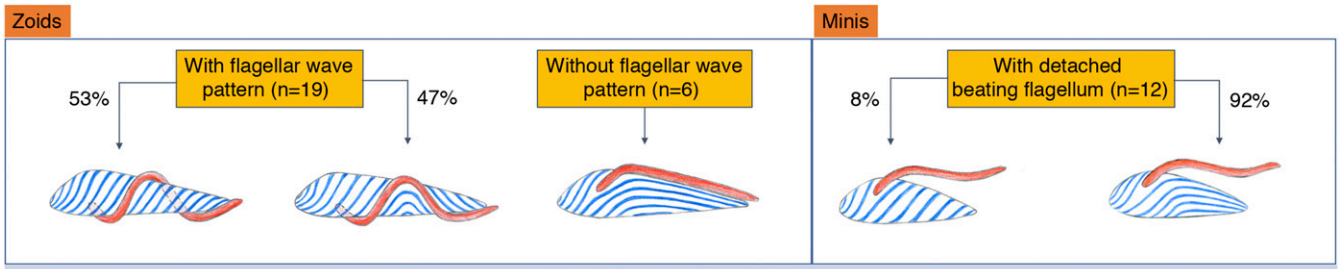

Handedness of flagellum				
Left only	Left/Right mixed	Left at posterior, no handedness toward the anterior	N/A	N/A
Handedness of subpellicular microtubules				
Left only	Left/Right mixed	Left at posterior, no handedness toward the anterior	Left only	Left at posterior, no handedness toward the anterior

Fig. 4. Handedness of SPM helical arrangement follows that of the flagellum in zoids. Twenty-five tomograms of randomly selected zoids and 12 tomograms of randomly selected minis were recorded, reconstructed, and annotated for the flagellum and cell body using manual annotation or the automated annotation tool in EMAN2. The helical arrangement of the flagellum around the cell body was characterized and listed in the table above. The SPMs were automatically annotated in both zoids and minis, and their handedness was analyzed.

flagellum (Fig. 4 and *SI Appendix*, Fig. S4). In contrast, more complex SPM helical arrangements were observed in over 25 tomograms of zoids with attached flagella. Importantly, SPMs in zoids mirrored the local helical arrangement of the flagellum, providing direct evidence that the cytoskeleton organization is coupled to flagellar configuration (Fig. 3*C* and Movie S3).

Based on flagellar morphology, the 25 zoid tomograms were classified into two types (*SI Appendix*, Fig. S4). Greater than three-quarters of zoids (19/25) had flagella exhibiting flagellar waves similar to those observed in live wild-type *T. brucei* (Fig. 2*C*), or in chemically fixed wild-type cells using scanning electron microscopy (SEM) (9). In the other one-quarter of zoids, the flagellum was nonhelical and appeared parallel to the cell body along the length of the attachment. As the cells represent snapshots of flagellar beating captured at the time of vitrification, this minority population could represent a particular functional state during the beating waveform or cells not undergoing flagellar beating.

Twenty-three of the 25 zoid tomograms could be annotated using the automated tomogram annotation method (30). In all 23, the SPMs in the region posterior to the flagellum attachment exhibited only left-handed helicity. In this respect, SPM in zoids resembled those in mini cells. However, SPM arrays located in the anterior part of the cell (i.e., where the flagellum is attached) followed the local handedness of their flagellum (Fig. 4). In zoids with a flagellar wave pattern, approximately one-half (47%) contained SPM and flagellar helices with mixed left- and right-handedness, and the other half (53%) contained SPM and flagella with only left-handed helical arrangements. By contrast, in zoids without a flagellar wave pattern, the SPM appeared nonhelical, like the flagellum. In summary, the SPMs followed the local helical pattern of the flagellum, with the exception of the posterior region. None of the 23 zoids had either all–left-handed flagella with mixed SPM handedness, or vice versa. These observations indicate that flagellar motility plays a role in modulating the helical patterns of SPMs and specifically implicates lateral flagellar attachment, which is present in zoids but not in mini cells.

The SPM Array Is a Deformable Scaffold. To further characterize the spatial organization of the SPM arrays, we quantified and visualized the center-to-center distance between adjacent SPMs (SPM spacing) by manually annotating a representative mini, a zoid with flagellar wave pattern, and a zoid without flagellar wave pattern (Fig. 5*A*). We found that the intermicrotubule spacing within each cell was highly variable (Fig. 5*B*). Differences in SPM spacing were localized to different regions of the cell. For instance, the zoid with a flagellar wave had many tightly packed SPMs with a spacing of <35 nm. However, these SPMs were mainly localized to two regions on either side of the flagellar wave (Fig. 5*A*) where the cell cross-section narrowed (*SI Appendix*, Fig. S5). To a lesser extent, reduced SPM spacing was also observed in the zoid without a flagellar wave in areas where the cell was in contact with the lacey carbon film of the electron microscopy support grid (Fig. 5*A*), suggesting that the SPM array is deformable not only by flagellar beating but also by external or environmental forces (i.e., the electron microscopy grid support film). Although the variations in intermicrotubule spacing we observed within each cell contrasts with previous reports describing this spacing as "invariant" in chemically fixed samples (31), the mean SPM spacing was similar between cells: 42 nm (SD, 19 nm) in the mini, 43 nm (SD, 17 nm) in the zoid with a flagellar wave, and 46 nm (SD, 16 nm) in the zoid without a flagellar wave. These mean spacing values are consistent with published values of spacing for chemically fixed and plastic-embedded wild-type cells (31).

Many eukaryotes, including *Trypanosoma*, have "cross-bridges" that span adjacent microtubules (21, 31). Where the SPM spacing varies, are cross-bridges absent, or can they stretch to different lengths? We extracted subvolumes containing microtubule segments and projected them normal to the plane of the SPM to create 2D "top views" of local regions. We sorted these by reference-free class averaging, yielding classes with larger or smaller spacing between neighboring SPM. Mapping the areas contributing to each width class back onto the raw tomogram (Fig. 5*C*), we confirmed the pattern observed from manual segmentation: for instance, tighter spacing on either side of the flagellar wave (Fig. 5*A*). In these classes, cross-bridges were observed regardless of the intermicrotubule spacing. As an alternative to reference-free class averaging, we then sorted projections into classes based on the spacing measured from manual segmentation of the SPM and obtained a similar result (Fig. 5*C*). Whether using reference-free or segmentation-based classification, the cross-bridge densities are found to occur periodically every 26.6 nm along the SPM (SD, 0.8) despite the large variation in intermicrotubule distance of SPMs from 28 to 53 nm (Fig. 5*E*).

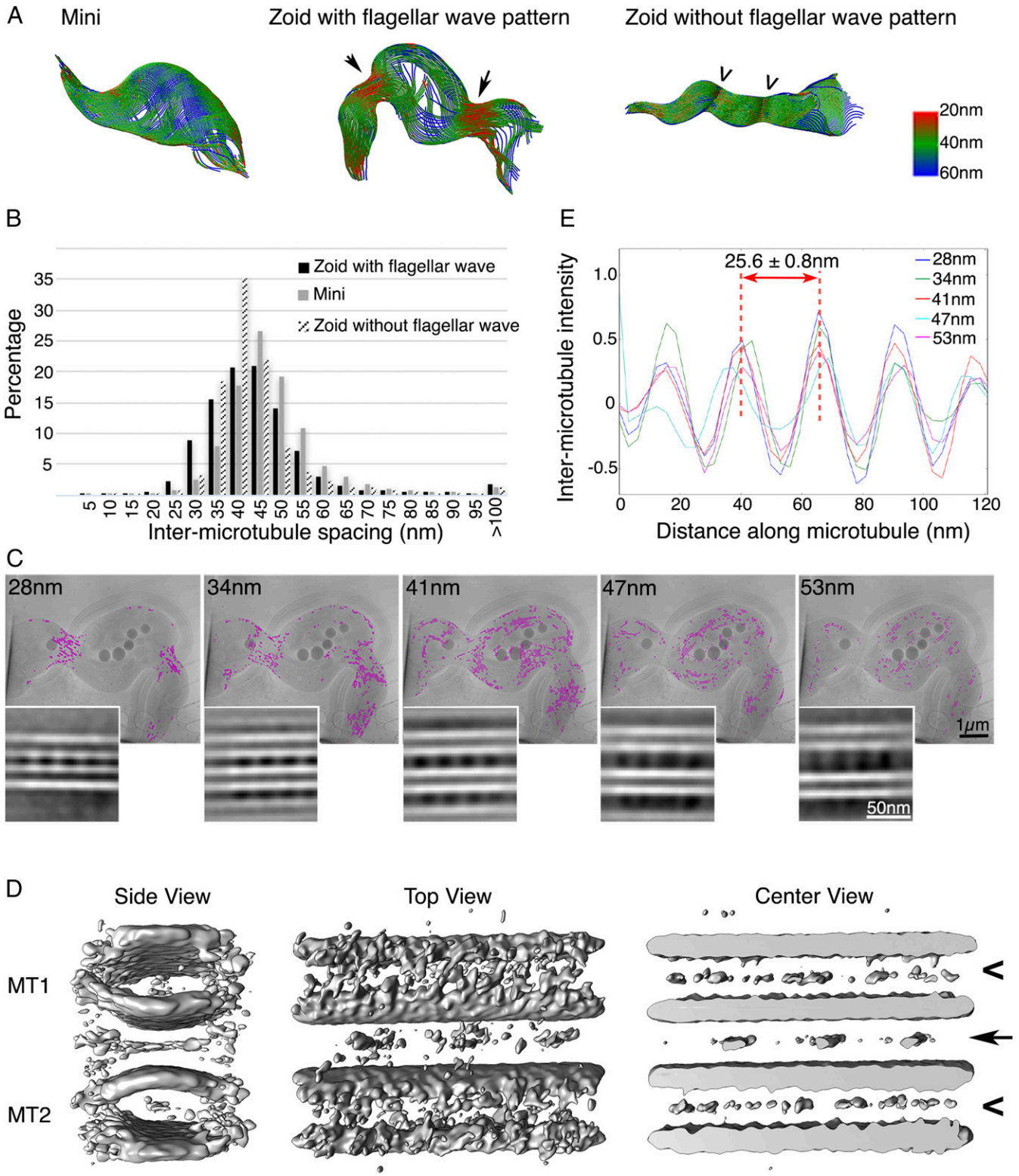

Fig. 5. Flagellar wave modifies SPM spacing. (*A* and *B*) Intermicrotubule spacing of representative minis and zoids, either with or without a flagellar wave, shown as heat maps (*A*) or histograms (*B*). The histogram indicates larger spacing in minis, while smaller spacing is more dominant in zoids, especially those with a flagellar wave (arrows in *A*) or in any part of the cell in close contact with the lacey grid (arrowheads, in *A*). (*C*) Microtubule segments were manually extracted from different parts of a single zoid that contained a flagellar wave, as shown in the *Middle* of *A*. Note that images shown in *C* were flipped horizontally compared with *A*. These segments were divided into five classes based on the intermicrotubule spacing. The cellular position of all segments belonging to that spacing class is marked in pink. An enlarged view of an average of the segments from that class is shown in an *Inset*. (*D*) Subtomogram averages of neighboring SPMs (denoted MT1 and MT2) revealed intramicrotubule densities (arrowheads) as well as intermicrotubule connecting densities (arrow). (*E*) The intensity and the position of the connecting density between adjacent SPMs were determined for all five classes.

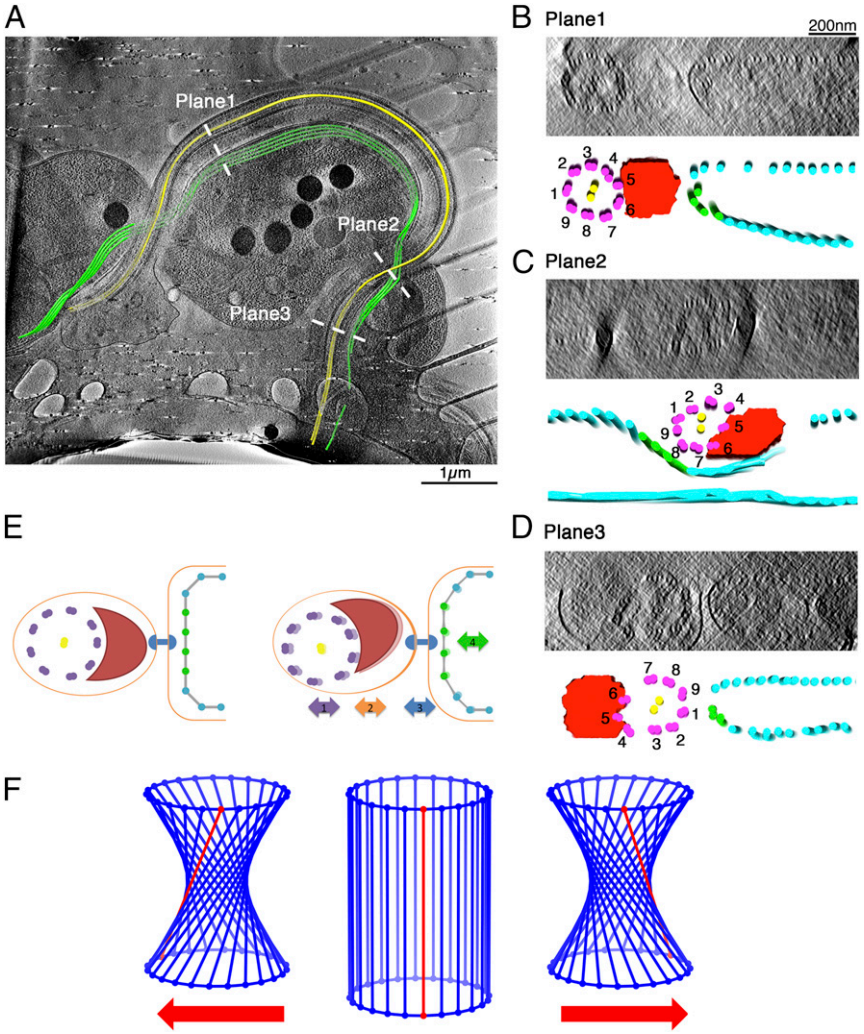

Fig. 6. A flexible connection between the axoneme and the SPM. (*A*) In this zoid containing a flagellar waveform, the flagellar axoneme (whose orientation is defined by the central pair microtubules in yellow) and the MtQ (part of the SPM array, and colored green) do not have the same relative orientation along the entire flagellar attachment region. (*B–D*) Cross-sections of the tomograms (*Top*) and 3D annotations (*Bottom*) at three different cross-sections marked in *A*. Although the relative position of the axoneme (doublets in pink and central pair in yellow) with respect to its PFR (red) remains constant, the entire flagellar complex (axoneme plus PFR) appears to rotate with respect to the MtQ. (Scale bars: 200 nm.) (*E*) Cartoon representation of key components in force transmission, colored as in *B–D*, relaxed (*Left*) or during axonemal bending (*Right*). The bending of the axoneme (purple), which is rigidly linked to the PFR (red), will push or pull the staples (blue) that connect the flagellar and cellular membranes (orange), but there is no rigid connection between the axoneme/PFR and the staple and the axonemal force may be transmitted to the staple via other flexible connections or the membrane itself. The SPM (blue), and its MtQ in particular (green), are twisted by this force and perhaps also pulled apart or pushed together causing variation in the span of cross-bridges (gray). Block arrows numbered 1–4 represent the order of force transmission from the axoneme to the axoneme/PFR complex (2), to the staples (3), and finally to the SPMs. (*F*) Model of a hyperboloid of revolution, showing how local cell deformation could be induced by flagellar beating (left and right turns) and external forces that limit rotation at the top of the hyperboloid.

We further confirmed this finding of cross-bridge spacing in 3D. We extracted subvolumes containing two neighboring SPM (denoted MT1 and MT2 in Fig. 5*D*) from a dataset of higher-magnification tomograms. Three-dimensional subtomogram averaging confirmed the presence of cross-bridges every 26.6 nm (Fig. 5*D*). Furthermore, we also noted densities inside the SPM (Fig. 5*D*), just as microtubule luminal densities have been observed in a variety of organisms (16, 32).

The Connection Between the Axoneme in the Flagellum and SPMs in the Cell Body Is Not Rigid. Because the cell body deforms in response to flagellar beating (Figs. 4 and 5), there must exist some set of molecules to mechanically couple the force of axonemal bending in the flagellum to the SPM cortex in the cell body. We observed the ultrastructural organization of the flagellar attachment region in zoids with or without a flagellar wave pattern, examining the relative positions of the PFR, axoneme, and MtQ along the entire length of flagellar attachment in all of the zoids (Fig. 6*A*). The relative position of the PFR to the axoneme was fixed, consistent with previous observations (33) (*SI Appendix*, Fig. S1). However, the position of the PFR/axoneme complex relative to the MtQ (and cell body) was highly variable. Whether a flagellar wave pattern was present or absent, the relative position of the PFR/axoneme complex with respect to the MtQ is not fixed—even within a single cell (compare Fig. 6*B* to Fig. 6*D*; *SI Appendix*, Fig. S6). The variable positioning of the PFR/axoneme complex relative to the SPM was also observed in transmission electron microscopy (TEM) sections of chemically fixed wild-type parasites and in ion beam slice views of wild-type cells fixed with high-pressure freezing and freeze substitution (*SI*

Appendix, Fig. S7), although the relative angles were not as extreme as those seen in the cryo-ET samples. For both serial-section TEM and focused ion beam (FIB) SEM, the samples were chemically fixed in suspension, therefore free of possible compression artifacts produced in the plunge-freeze protocol of cells. These results suggested that the macromolecules connecting the axonemal microtubules and SPM are not spatially rigid, contrary to previous models that assumed a rigid connection (8).

Discussion

In this study, we generated genetically anucleate *T. brucei* mutants that differ in flagellar attachment and motility phenotypes. Cryo-ET of the anucleate zoids provided an ensemble of structural snapshots of the cytoskeleton and associated flagellum in different cell motility states of *T. brucei* as indicative by their wave patterns. By comparing zoids and minis with and without lateral flagellar attachment (Fig. 3), we showed that the cell body itself can deform as defined by changes in SPM helicity (Fig. 4) and spacing (Fig. 5) in response to flagellar beating and external conditions as reflected by the wave patterns and EM grid support surface. The flagellar motility-dependent cell deformation may explain the extraordinary ability of live *T. brucei* cells to penetrate size-limiting slits in microfluidic devices (Fig. 1).

The observation of cell deformation, as defined by handedness changes and spacing variation of the SPMs, requires the ability to visualize and analyze whole-cell microtubule organizations at nanometer resolution. This was achieved in our study using cryo-ET on anucleate *T. brucei.* Previous EM studies with thin sections or cryosections did not systematically measured microtubule spacing in whole cells. In published studies, serial block face–SEM, cryo-soft X-ray tomography, or live-cell optical imaging have been used to view whole *T. brucei* cells, vitrified or live. However, these techniques do not have the resolution to see individual microtubules in whole cells (18, 34). In our cryo-ET study, we additionally observed a "constriction site," presented by the reduction in SPM spacing and cross-section area, in the cell body of ∼40% zoids imaged but never in minis (Fig. 5 and *SI Appendix*, Figs. S4 and S5). In all zoids containing a constriction site, flagellar waves were present. This type of cell deformation has not been reported in other whole-cell reconstruction studies (18, 35); neither was this deformation observed in our own slice-and-view reconstructions of suspension cells preserved by high-pressure freezing (*SI Appendix*, Fig. S7). Notably, the flexibility in the axoneme/MtQ positioning in zoids was confirmed through other EM sample preparation protocols and imaging techniques by using standardized chemical fixation, hydration, and embedding followed by ultrathin sectioning or using high-pressure freezing followed with FIB-SEM (Fig. 6 and *SI Appendix*, Figs. S6 and S7). Both protocols were applied to cell suspensions.

The absence of evidence for a constriction site and cell deformation in high-speed video of live-cell studies (9), our FIB-SEM, or other whole-cell reconstruction studies (18, 35) suggested that the extreme cell deformation may be present in some cells plunge-frozen on grids but not in free-swimming cells. Cells plunge-frozen for cryo-ET differ in two major ways from chemically fixed or high-pressure frozen cells. First, the force of blotting may compress cells, potentially introducing nonnatural deformations. Second, contact with the grid surface may impose additional forces on the trypanosome samples. In either scenario, the additional environmental forces may limit the free movement and rotation of the cell body. In particular, if flagellar beating twists the SPMs while cell body rotation is restricted, a hyperboloid would be introduced and constriction would result (Fig. 6*F* and Movie S5). Based on these results, cell body deformation observed in cryo-ET (but not in other imaging methods on cell suspensions) is likely a consequence of flagellar beating during blotting combined with trypanosome interaction with the grid.

Past and recent studies have noted a highly invasive lifestyle of *T. brucei*, which is capable of penetrating deeply into various tissues and organs in the hosts. For example, *T. brucei* penetrates the blood–brain barrier in animal hosts and can be found in many deep tissues (36, 37). In tsetse flies, it can penetrate the peritrophic matrix and the proventriculus to migrate from the midgut to the salivary gland (38). Such penetration behavior would involve close contact and interaction of *T. brucei* with host cells and tissues. Thus, the cell deformation phenotypes we observed in the microfluidic and the cryo-ET experiments may be relevant to the configuration of *T. brucei* in a host, and the deformability of SPMs and the cell body may be critical for parasite penetration through size-limiting barriers in the host. Indeed, *T. brucei* contact with host cells and tissues has long been documented, both in vitro and in vivo (39, 40).

Only a few studies, however, have examined the role of flagellar motility in host infections. In tsetse flies, a motility mutant can proliferate in the midgut but cannot establish salivary gland infections, suggesting that this motility mutant fails to migrate from midgut to salivary gland or cannot differentiate from procyclic form to other life cycle stages (41). In mice, a PFR mutant was rapidly cleared from infected animals (42). However, a dynein mutant that does not exhibit viscosity-dependent motility enhancement (but is otherwise viable in culture) infects mice as efficiently as wild-type cells (43). These in vivo studies manifest the complexity of the function and regulation of flagellar motility. Different flagellum-dependent cellular functions are likely differentially required for various infection needs.

We have previously shown that the sinusoidal axonemal bending can be transformed into a 3D bihelical pattern by the PFR (44). Here, we demonstrated that the relative position of the axoneme/PFR complex with respect to the MtQ is highly variable (Fig. 6 *B* and *D* and *SI Appendix*, Fig. S6). We thus propose that the axoneme/PFR complex pushes or pulls its enveloping flagellar membrane or some other flexible linker proteins to transmit force to the staple-like structures in the attachment zone. This force distorts the SPM array. The distortion leads primarily to SPM array twisting, which dictates the handedness when flagella are attached to the cell body. This mechanical model explains how axonemal bending force can twist the cell body (Fig. 6*E*). Note that both left-handed and right-handed helical arrangement of both the flagellum and the SPMs have been observed in our reconstructed zoids in contact with electron microscopy grids. These ultrastructural results are consistent with the bihelical motion model (9) previously proposed for procyclic cell motions in suspension. It is worth noting that our study is performed exclusively on mutants derived from procyclic cells. Several differences in motility behavior have been noted between procyclic and bloodstream-form parasites. For example, procyclic cells demonstrate social motility behavior which is not observed in bloodstream-form cells under the same conditions (13). The bloodstream-form cells (8), but not the procyclic cells (*SI Appendix*, Table S1), show enhanced swimming directionality and persistence in high-viscosity medium. It is possible that procyclic and bloodstream-form flagella have different beating motions. Nevertheless, any of these motions are based on the underlying biophysical properties as revealed here in terms of the handedness and microtubule spacing changes.

Recent studies have made remarkable progress in identifying the molecular components that connect the flagellum to the cell body, mostly in the procyclic-form cells (3, 5, 6, 26, 45–48). High–molecular-mass molecules such as FLAM3 have been proposed to connect the axoneme to the FLA1BP/FLA1 membrane adhesion structure (46). How these molecules interact and function together to link the flagellum to the SPM is yet to be investigated. In particular, the staple's components are unidentified. Previously, we showed that the flagellar transmembrane protein FLA1BP interacts with cell membrane protein FLA1 via their extracellular

domains, and FLA1BP and FLA1 are both required for proper flagellar attachment (26). Here, when we silence FLA1BP, we no longer observe staples nor cell deformation in minis (Figs. 2 and 4). Taken together, these results indicate that either FLA1BP is a key component or is required for formation or stability of the staples, which are crucial structural components in force transmission from the flagellum to the cell body.

Materials and Methods

Cell Culture and Transfection. The procyclic *T. brucei* cell line 29.13, which is engineered to support tetracycline-inducible expression, was cultivated in Cunningham's medium (49) supplemented with 15% heat-inactivated tetracycline-free FBS (Clontech Laboratories),15 μg/mL G418, and 50 μg/mL hygromycin at 28 °C. RNAi silencing of FLA1BP and TbCentrin4 were performed as previously described (26, 29). For dual silencing of FLA1BP and TbCentrin4, we cloned a 420-bp fragment of TbCentrin4 (nucleotides 19–438) and a 518-bp fragment of FLA1BP (nucleotides 1385–1902) into a pZJM construct (50) (called pZJM/FLA1BP-TbCentrin4). For stable transfection, 15 μg of NotI-linearized plasmid DNA was electroporated into cells, and stable clones were selected with phleomycin (10 μg/mL) via serial dilution.

Microfluidic Methods. The microfluidic device consisted of 24 rows of hexagonal constrictions with a slit size of 1.4 μm (*SI Appendix*, Fig. S2). Bypass channels were designed on both sides of the constriction channel to prevent cell overload and sudden changes of flow. To prepare the microfluidic devices, a master mold was fabricated on an SU-8 photoresist. The microfluidic devices were fabricated with a 10:1 ratio of polydimethylsiloxane (PDMS) to curing agent using a standard soft lithography technique. An inlet and outlet was created using a 1.2-mm puncher. The prepared microfluidic devices were permanently attached to glass slides after plasma (FemtoScientific) and heat treatment. To perform the experiment, a microfluidic device was mounted onto an Olympus X71 microscope stage and observed using a 60× objective. A PHD Ultra (Harvard Apparatus) syringe pump was attached to the device using Tygon tubing. Before loading the cells, the chambers were washed with PBS containing 1% BSA at a flow rate of 25 μL/min to reduce friction between cells and constrictions. An estimated 8×10^6 cells were loaded into a 1-mL syringe and injected into the microfluidic device at a flow rate of 5 μL/min. Once initiated, the system stabilized after 5 min, and then flowing cells were recorded at a rate of 100 frames per s (fps) using a Phantom V9.1 high-speed camera (Vision Research Phantom) for 13 s per video. Using the recorded videos, we calculated the percentage of cells that passed through 10 or more constrictions within the 13-s recording time. For the cells that transited at least 10 slits, we calculated the length of time required to pass through all 10 slits. Trypanosome tracking was performed automatically using customized scripts. The average of all video frames was subtracted from each frame so all moving objects could be identified. Objects that were close to each other in adjacent frames in the video were connected to form paths of trypanosome movement. Speed of cell movement was estimated using the distance the trypanosome moved from the previous frame to the next frame.

Isolation of Minis and Zoids. Dual FLA1BP-Centrin4-RNAi or Centrin4-RNAi cells were cultured with 10 μg/mL tetracycline for 60 h to generate mini cells or zoids, respectively. Cells were pelleted by centrifugation at 1,800 × *g* for 7 min and resuspended in serum-free media. Anucleate cells were enriched by centrifuging at low speed three times using a swinging-bucket rotor (Eppendorf 5417R, Rotor A-8-11) and retaining only the top portion of the supernatant after each round of centrifugation. The protocol for each round of centrifugation was as follows: (*i*) 500 rpm for 2 min, 800 rpm for 2 min, then 1,400 rpm for 5 min and retaining 35% of the supernatant; (*ii*) 800 rpm for 3 min, then 1,500 rpm for 5 min and retaining 55% of the supernatant; and (*iii*) 1,800 rpm for 3 min and retaining 60% of the supernatant, which was highly enriched with zoids or mini cells (>70% homogeneity).

Light Microscopy. Cells were attached to coverslips, fixed, and permeabilized with prechilled methanol at −20 °C for 15 min and blocked with 3% BSA in PBS for 1 h before immunolabeling. Anti-PFR1 (51) and monoclonal antibody L3B2 (52) were used to label the PFR and the flagellum attachment complex, respectively. Nuclear and kinetoplast DNA was counterstained with 2 μg/mL DAPI (D1306; Invitrogen). Images or *Z* stacks (7–10 optical slices in 0.5-μm steps covering the entire cell depth) were acquired using an Axioplan2 inverted microscope (Carl Zeiss MicroImaging) equipped with a CoolSNAP HQ^2 camera (Photometrics) and a Plan-Apochromat 63×, N.A. 1.4 oil objective. Image processing and analyses were performed using AxioVision, release 4.8 (Carl Zeiss), for maximum intensity presentations of *z* stacks, ImageJ with ROI manager or MTrackJ plugin for length/distance measurements (53), and Adobe Photoshop CC 2015.5 for figure preparation.

Live-Cell Imaging. Control and freshly prepared mini cells or zoids were maintained in Cunningham's medium at 28 °C until imaging. To track cell movement, 10 μL of culture were spotted onto a hemocytometer and imaged using a 20× objective at 5 or 6 fps for 10 s. Cell movement was tracked by marking the position of the cell's posterior end in each frame in ImageJ. To monitor persistent swimming behavior, we calculated the percentage of cells that moved >80 μm in any single direction during the 10-s imaging period over the total cells seen in the movies. To monitor flagellar beating (~17 Hz), cells were imaged at 1,000 fps using a Phantom v9 camera (VisionResearch) for at least 1 s. Unlike the bloodstream form of *T. brucei* that exhibit viscosity-dependent motility behavior (8, 54), modification of medium viscosity using methylcellulose did not significantly affect the motility of the procyclic form of wild-type parasites (*SI Appendix*, Table S1). Thus, all subsequent cell motility assays in this study were performed in culture medium.

Cryo-ET of Plunge-Frozen Cells. For whole-cell cryo-ET, 2 μL of zoids or mini cells (~3×10^6 cells per mL) were spread on lacey carbon film across copper EM grids (LC200-Cu-25, 200 mesh; Electron Microscopy Sciences). We added 2 μL of 25-nm gold particles to each side of the grids before and after cell attachment. Excess medium was blotted off in an environmentally controlled chamber maintained at 22 °C and 100% humidity. Cells were rapidly fixed by plunging into liquid ethane with Vitrobot Mark IV (FEI Company). Grids were stored in liquid nitrogen until cryo-ET examination.

To exclude cells that might be compressed or disrupted by blotting and freezing, samples for cryo-ET data collection were screened to search for intact cells positioned over the holes of the lacey film. Most tomograms were recorded on a Titan Krios electron microscope (FEI Company) at 300 kV equipped with a Falcon 2 direct detector. Tomographic tilt series were collected between ±60° at 1° or 2° increments with a defocus of −10 or −15 μm and different magnifications corresponding to 5.3 or 21.4 Å/pixel, respectively. Data were acquired under low-dose conditions using FEI tomography software (FEI Company). The exposure was ~0.3 $e^-/Å^2$ per image, and the accumulated exposure for each tilt series was ~40 $e^-/Å^2$ per tomogram.

Some tomograms were recorded on a 200-kV JEM2200FS equipped with an in-column energy filter and a slit set to 20 eV. Tilt series were collected under low-dose conditions using SerialEM (55). The series was collected between ±60° in 1.5° increments with a targeted defocus of −10 μm and magnification of 8,000×, equivalent to 15.2 Å/pixel using a Gatan US4000 CCD camera. The dose rate was ~2.6 $e^-/Å^2$ per s, and exposure time was 0.5 s. The original images were binned 2 × 2. Tilt series were reconstructed using IMOD (56).

Tomogram Analysis. In the tomograms of three representative zoids and mini (Figs. 3, 5, and 6), PFR was manually annotated with Avizo (Visualization Sciences Group, FEI), and microtubules and all other organelles were annotated manually using IMOD (56). Using SciPy, annotations were oversampled and nearest-neighbor distances were computed using a *k*-d tree. For class averaging, microtubule subvolumes were extracted based on manual annotation. Aligned subvolumes were projected normal to the cell surface and sorted using reference-free class averaging to identify classes with larger or smaller spacing between neighboring SPMs. The normal vector was approximated using information from manual annotation, specifically the local vector of the microtubule and the direction of nearest neighbors. Projections underwent reference-free classification and were averaged iteratively using EMAN2 (57). Separately, projections were classified based on the spacing between the microtubules, which was estimated from manual annotation.

In the other zoids and minis, microtubules were annotated using the automated annotation tool in EMAN2 (30); the helical handedness was scored by eye based on the segmentation. To visualize the density between microtubules, microtubule subvolumes were extracted from an automatically annotated zoid imaged at 5.3 Å/pixel. Subvolume projections were used to perform an initial alignment and generate an initial model. Particles were aligned and averaged using EMAN2 single-particle tomography tools (58).

TEM. For TEM, 29.13 cells in suspension were fixed in situ with 2.5% glutaraldehyde in PBS, pH 7.2, and postfixed with 1% OsO_4. After dehydration through increasing concentrations of ethanol, the samples were embedded in Spurr's resin. Ultrathin sections were stained with 0.2% uranyl acetate, air-dried, and then viewed using a Tecnai 12 electron microscope (FEI).

Dual-Beam Slice-and-View. Highly concentrated 29.13 cells were fixed by high-pressure freezing at 2,100 bar (Technotrade International) and freeze substituted with 1% OsO_4 and 0.05% uranyl acetate in acetone in liquid nitrogen in a Leica EM AF S2 system for 48 h at −90 °C, 24 h at −60 °C, 18 h at −30 °C, and 4 h at 0 °C. Samples were then infiltrated and polymerized with LX112 resin (Ladd Research Industries), and viewed using a Helios Dual Beam system (FEI).

ACKNOWLEDGMENTS. We thank Darius Jonasch for assistance with figure preparation and Htet Khant for technical support. This research was supported by grants from the Singapore Ministry of Education Tier 1 and Tier 2 Grants (R-154-000-A30-114 and MOE2013-T2-1-092), Mechanobiology Institute at the National University of Singapore, National Institutes of Health Grants P41GM103832 and R01GM080139, and Robert Welch Foundation Grant Q1242.

1. Hotez PJ, et al. (2007) Control of neglected tropical diseases. *N Engl J Med* 357: 1018–1027.
2. Langousis G, Hill KL (2014) Motility and more: The flagellum of *Trypanosoma brucei*. *Nat Rev Microbiol* 12:505–518.
3. Sunter JD, et al. (2015) Modulation of flagellum attachment zone protein FLAM3 and regulation of the cell shape in *Trypanosoma brucei* life cycle transitions. *J Cell Sci* 128: 3117–3130.
4. Sunter JD, Varga V, Dean S, Gull K (2015) A dynamic coordination of flagellum and cytoplasmic cytoskeleton assembly specifies cell morphogenesis in trypanosomes. *J Cell Sci* 128:1580–1594.
5. Zhou Q, Liu B, Sun Y, He CY (2011) A coiled-coil- and C2-domain-containing protein is required for FAZ assembly and cell morphology in *Trypanosoma brucei*. *J Cell Sci* 124: 3848–3858.
6. Zhou Q, Hu H, He CY, Li Z (2015) Assembly and maintenance of the flagellum attachment zone filament in *Trypanosoma brucei*. *J Cell Sci* 128:2361–2372.
7. LaCount DJ, Barrett B, Donelson JE (2002) *Trypanosoma brucei* FLA1 is required for flagellum attachment and cytokinesis. *J Biol Chem* 277:17580–17588.
8. Heddergott N, et al. (2012) Trypanosome motion represents an adaptation to the crowded environment of the vertebrate bloodstream. *PLoS Pathog* 8:e1003023.
9. Rodríguez JA, et al. (2009) Propulsion of African trypanosomes is driven by bihelical waves with alternating chirality separated by kinks. *Proc Natl Acad Sci USA* 106: 19322–19327.
10. Alizadehrad D, Krüger T, Engstler M, Stark H (2015) Simulating the complex cell design of *Trypanosoma brucei* and its motility. *PLoS Comput Biol* 11:e1003967.
11. Wheeler RJ (2017) Use of chiral cell shape to ensure highly directional swimming in trypanosomes. *PLoS Comput Biol* 13:e1005353.
12. Gadelha C, Wickstead B, Gull K (2007) Flagellar and ciliary beating in trypanosome motility. *Cell Motil Cytoskeleton* 64:629–643.
13. Oberholzer M, Lopez MA, McLelland BT, Hill KL (2010) Social motility in african trypanosomes. *PLoS Pathog* 6:e1000739.
14. Lučič V, Rigort A, Baumeister W (2013) Cryo-electron tomography: The challenge of doing structural biology in situ. *J Cell Biol* 202:407–419.
15. Henderson GP, Gan L, Jensen GJ (2007) 3-D ultrastructure of *O. tauri*: Electron cryotomography of an entire eukaryotic cell. *PLoS One* 2:e749.
16. Cyrklaff M, et al. (2007) Cryoelectron tomography reveals periodic material at the inner side of subpellicular microtubules in apicomplexan parasites. *J Exp Med* 204: 1281–1287.
17. Wang R, et al. (2015) Electron cryotomography reveals ultrastructure alterations in platelets from patients with ovarian cancer. *Proc Natl Acad Sci USA* 112:14266–14271.
18. Hughes L, Borrett S, Towers K, Starborg T, Vaughan S (2017) Patterns of organelle ontogeny through a cell cycle revealed by whole-cell reconstructions using 3D electron microscopy. *J Cell Sci* 130:637–647.
19. Yelinek JT, He CY, Warren G (2009) Ultrastructural study of Golgi duplication in *Trypanosoma brucei*. *Traffic* 10:300–306.
20. de Souza W, Attias M (2010) Subpellicular microtubules in apicomplexa and trypanosomatids. *Structures and Organelles in Pathogenic Protists*, ed de Souza W (Springer, Berlin).
21. Hemphill A, Lawson D, Seebeck T (1991) The cytoskeletal architecture of *Trypanosoma brucei*. *J Parasitol* 77:603–612.
22. Sherwin T, Gull K (1989) The cell division cycle of *Trypanosoma brucei brucei*: Timing of event markers and cytoskeletal modulations. *Philos Trans R Soc Lond B Biol Sci* 323: 573–588.
23. Ralston KS, Kabututu ZP, Melehani JH, Oberholzer M, Hill KL (2009) The *Trypanosoma brucei* flagellum: Moving parasites in new directions. *Annu Rev Microbiol* 63:335–362.
24. Höög JL, Bouchet-Marquis C, McIntosh JR, Hoenger A, Gull K (2012) Cryo-electron tomography and 3-D analysis of the intact flagellum in *Trypanosoma brucei*. *J Struct Biol* 178:189–198.
25. Reddy GS, Mukhopadhyay AG, Dey CS (2017) Characterization of ciliobrevin A mediated dynein ATPase inhibition on flagellar motility of *Leishmania donovani*. *Mol Biochem Parasitol* 214:75–81.
26. Sun SY, Wang C, Yuan YA, He CY (2013) An intracellular membrane junction consisting of flagellum adhesion glycoproteins links flagellum biogenesis to cell morphogenesis in *Trypanosoma brucei*. *J Cell Sci* 126:520–531.
27. Robinson DR, Sherwin T, Ploubidou A, Byard EH, Gull K (1995) Microtubule polarity and dynamics in the control of organelle positioning, segregation, and cytokinesis in the trypanosome cell cycle. *J Cell Biol* 128:1163–1172.
28. Brasseur A, et al. (2014) The bi-lobe-associated LRRP1 regulates Ran activity in *Trypanosoma brucei*. *J Cell Sci* 127:4846–4856.
29. Shi J, et al. (2008) Centrin4 coordinates cell and nuclear division in *T. brucei*. *J Cell Sci* 121:3062–3070.
30. Chen M, et al. (2017) Convolutional neural networks for automated annotation of cellular cryo-electron tomograms. *Nat Methods* 14:983–985.
31. Lacomble S, et al. (2009) Three-dimensional cellular architecture of the flagellar pocket and associated cytoskeleton in trypanosomes revealed by electron microscope tomography. *J Cell Sci* 122:1081–1090.
32. Garvalov BK, et al. (2006) Luminal particles within cellular microtubules. *J Cell Biol* 174:759–765.
33. Bastin P, Matthews KR, Gull K (1996) The paraflagellar rod of kinetoplastida: Solved and unsolved questions. *Parasitol Today* 12:302–307.
34. Luengo I, et al. (2017) SuRVoS: Super-region volume segmentation workbench. *J Struct Biol* 198:43–53.
35. Weber B, et al. (2014) Automated stitching of microtubule centerlines across serial electron tomograms. *PLoS One* 9:e113222.
36. Mulenga C, Mhlanga JD, Kristensson K, Robertson B (2001) *Trypanosoma brucei brucei* crosses the blood-brain barrier while tight junction proteins are preserved in a rat chronic disease model. *Neuropathol Appl Neurobiol* 27:77–85.
37. Anosa VO, Kaneko JJ (1983) Pathogenesis of *Trypanosoma brucei* infection in deer mice (*Peromyscus maniculatus*): Hematologic, erythrocyte biochemical, and iron metabolic aspects. *Am J Vet Res* 44:639–644.
38. Rotureau B, Van Den Abbeele J (2013) Through the dark continent: African trypanosome development in the tsetse fly. *Front Cell Infect Microbiol* 3:53.
39. Molyneux DH (1977) Vector relationships in the Trypanosomatidae. *Adv Parasitol* 15: 1–82.
40. Tetley L, Vickerman K (1985) Differentiation in *Trypanosoma brucei*: Host-parasite cell junctions and their persistence during acquisition of the variable antigen coat. *J Cell Sci* 74:1–19.
41. Rotureau B, Ooi CP, Huet D, Perrot S, Bastin P (2014) Forward motility is essential for trypanosome infection in the tsetse fly. *Cell Microbiol* 16:425–433.
42. Griffiths S, et al. (2007) RNA interference mutant induction in vivo demonstrates the essential nature of trypanosome flagellar function during mammalian infection. *Eukaryot Cell* 6:1248–1250.
43. Kisalu NK, Langousis G, Bentolila LA, Ralston KS, Hill KL (2014) Mouse infection and pathogenesis by *Trypanosoma brucei* motility mutants. *Cell Microbiol* 16:912–924.
44. Koyfman AY, et al. (2011) Structure of *Trypanosoma brucei* flagellum accounts for its bihelical motion. *Proc Natl Acad Sci USA* 108:11105–11108.
45. Nozaki T, Haynes PA, Cross GA (1996) Characterization of the *Trypanosoma brucei* homologue of a *Trypanosoma cruzi* flagellum-adhesion glycoprotein. *Mol Biochem Parasitol* 82:245–255.
46. Rotureau B, et al. (2014) Flagellar adhesion in *Trypanosoma brucei* relies on interactions between different skeletal structures in the flagellum and cell body. *J Cell Sci* 127:204–215.
47. Vaughan S, Kohl L, Ngai I, Wheeler RJ, Gull K (2008) A repetitive protein essential for the flagellum attachment zone filament structure and function in *Trypanosoma brucei*. *Protist* 159:127–136.
48. Moreira BP, Fonseca CK, Hammarton TC, Baqui MM (2017) Giant FAZ10 is required for flagellum attachment zone stabilization and furrow positioning in *Trypanosoma brucei*. *J Cell Sci* 130:1179–1193.
49. Kaminsky R, Beaudoin E, Cunningham I (1988) Cultivation of the life cycle stages of *Trypanosoma brucei* sspp. *Acta Trop* 45:33–43.
50. Wang Z, Morris JC, Drew ME, Englund PT (2000) Inhibition of *Trypanosoma brucei* gene expression by RNA interference using an integratable vector with opposing T7 promoters. *J Biol Chem* 275:40174–40179.
51. Gheiratmand L, Brasseur A, Zhou Q, He CY (2013) Biochemical characterization of the bi-lobe reveals a continuous structural network linking the bi-lobe to other single-copied organelles in *Trypanosoma brucei*. *J Biol Chem* 288:3489–3499.
52. Kohl L, Sherwin T, Gull K (1999) Assembly of the paraflagellar rod and the flagellum attachment zone complex during the *Trypanosoma brucei* cell cycle. *J Eukaryot Microbiol* 46:105–109.
53. Schneider CA, Rasband WS, Eliceiri KW (2012) NIH image to ImageJ: 25 years of image analysis. *Nat Methods* 9:671–675.
54. Bargul JL, et al. (2016) Species-specific adaptations of trypanosome morphology and motility to the mammalian host. *PLoS Pathog* 12:e1005448.
55. Mastronarde DN (2005) Automated electron microscope tomography using robust prediction of specimen movements. *J Struct Biol* 152:36–51.
56. Kremer JR, Mastronarde DN, McIntosh JR (1996) Computer visualization of three-dimensional image data using IMOD. *J Struct Biol* 116:71–76.
57. Tang G, et al. (2007) EMAN2: An extensible image processing suite for electron microscopy. *J Struct Biol* 157:38–46.
58. Galaz-Montoya JG, et al. (2016) Alignment algorithms and per-particle CTF correction for single particle cryo-electron tomography. *J Struct Biol* 194:383–394.